


Article

Investigations of Thermal, Mechanical, and Gas Barrier Properties of PA11-SiO₂ Nanocomposites for Flexible Riser Application

Jihong Wen ¹, Dong Huang ¹, Yan Li ², Xichong Yu ², Xinpeng Zhang ¹, Xiaoyu Meng ¹, Chuanbo Cong ¹ and Qiong Zhou ^{1,*}

¹ New Energy and Material College, China University of Petroleum, Beijing 102249, China

² Key Laboratory of Deepwater Engineering, CNOOC Research Institute Co., Ltd., Beijing 100027, China

* Correspondence: zhouqiong@cup.edu.cn

Abstract: Acidic gas penetration through the internal pressure sheath of a flexible riser tends to cause a corrosive environment in the annulus, reducing the service life of the flexible riser. Nanoparticles can act as gas barriers in the polymer matrix to slow down the gas permeation. Herein, we prepared PA11/SiO₂ composites by the melt blending method. The effect of adding different amounts of SiO₂ to PA11 on its gas barrier properties was investigated by conducting CO₂ permeation tests between 20 °C and 90 °C. As the temperature increased, the lowest value of the permeability coefficient that could be achieved for the PA11 with different contents of SiO₂ increased. The composites PA/0.5% SiO₂ and PA/1.5% SiO₂ had the lowest permeation coefficients in the glassy state (20 °C) and rubbery state (≥50 °C). We believe that this easy-to-produce industrial PA/SiO₂ composite can be used to develop high-performance flexible riser barrier layers. It is crucial for understanding riser permeation behavior and enhancing barrier qualities.



Citation: Wen, J.; Huang, D.; Li, Y.; Yu, X.; Zhang, X.; Meng, X.; Cong, C.; Zhou, Q. Investigations of Thermal, Mechanical, and Gas Barrier Properties of PA11-SiO₂ Nanocomposites for Flexible Riser Application. *Polymers* **2022**, *14*, 4260. <https://doi.org/10.3390/polym14204260>

Academic Editor: Xianyong Lu

Received: 2 September 2022

Accepted: 8 October 2022

Published: 11 October 2022

Publisher's Note: MDPI stays neutral with regard to jurisdictional claims in published maps and institutional affiliations.



Copyright: © 2022 by the authors. Licensee MDPI, Basel, Switzerland. This article is an open access article distributed under the terms and conditions of the Creative Commons Attribution (CC BY) license (<https://creativecommons.org/licenses/by/4.0/>).

Keywords: PA11; SiO₂; permeability; flexible riser

1. Introduction

Flexible risers are connecting pipelines that transport oil and gas from the seabed to the ground, which plays a key role in oil and gas development [1]. During the operation of the flexible risers, the internal fluid of the risers contains lots of acidic gases (CO₂, H₂S), as well as gas-phase water, which penetrates from the inner pressure sheath into the area between the inner and outer sheaths, a space known as the permeation annulus (Figure 1). Meanwhile, condensate or seawater can penetrate the annular space due to damage of the outer sheaths during installation. The highly corrosive environment caused by water and acidic gases poses a serious challenge to the selection of long-life internal pressure sheaths materials [2–4].

Commonly used polymers for internal pressure sheaths include polyamide-11 (PA11), polyvinylidene fluoride (PVDF), high-density polyethylene (HDPE), and cross-linked polyethylene (XLPE), with PA11 being the most used of the numerous materials [5]. Polyamides have good all-around properties and are one of the high-performance engineering plastics [6]. PA11 possesses outstanding mechanical characteristics (such as high fatigue resistance, a low frictional coefficient, and excellent creep resistance) and is widely used as a candidate material for flexible riser liners [7]. It also has high impact strength and remarkable chemical resistance [8], and has been used in multiple applications, including offshore pipelines, cables, automobiles, electroactive polymer actuators, and sensors [7–10]. However, PA11 needs to be modified to further improve the barrier property and to alleviate the disadvantage of poor heat resistance.

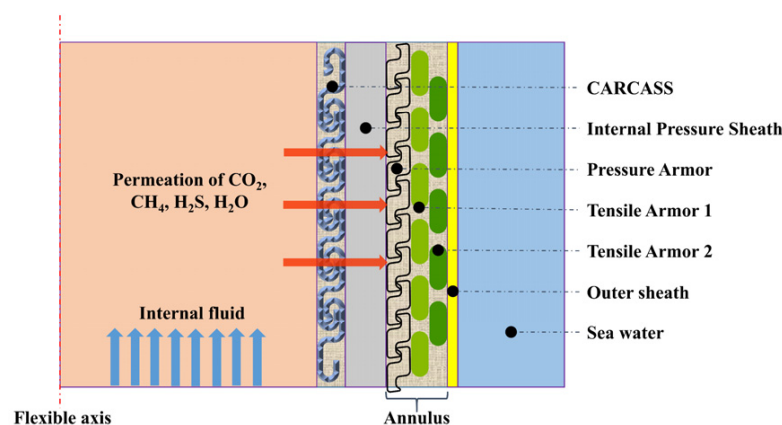


Figure 1. Permeation in the flexible riser.

Polymer-based nanocomposites have been extensively explored for the numerous innovative and remarkable features that nanoparticles can provide to polymers [11–14]. Previous studies have shown that the performance of PA11 can be improved by nanoparticle modification [7,15]. In the flexible riser field, the elastic modulus and the hardness parameters of the PA11 matrix were enhanced by the addition of montmorillonite (MMT) [16]. The concentration of 1.0 wt.% of commercial graphene nanoplatelets (GNP) promoted improvements in the thermal and mechanical properties of PA11 [17]. Among many inorganic nanoparticles, SiO₂ has been widely studied, due to its low price, easy availability, and high surface area. The PA11/SiO₂ nanocomposite coatings with nominal 15 vol% hydrophobic silica attained an enhancement in scratch resistance by 35% and wear resistance by 67% compared to neat polymer coatings [15]. Although some researchers have studied the effect of different nanoparticles on polymer permeability [18–21], a single nanoparticle ratio and a single test temperature cannot accurately reflect the mechanism of nanoparticle influence on the barrier behavior of polymer-based nanocomposites.

In this paper, PA11/SiO₂ (sphere, 25 nm, 100 m²/g) composites synthesized with different ratios were prepared by melt blending to evaluate their potential application in oil and gas pipelines. The CO₂ permeability of the PA11/SiO₂ composites at different temperatures was measured to explore the mechanism of the effect of different nanoparticle ratios on the permeation behavior of the polymer matrix. The results of the study are important for understanding riser permeation behavior and improving barrier properties, and can provide a reference for the prediction of the flexible riser annulus under various working circumstances.

2. Materials and Methods

2.1. Materials

Polyamide 11 resin (PA11, Rilsan[®] BESNO P4) was supplied by Arkema (Suzhou, China). Hydrophobic gas-phase SiO₂ powder (sphere) with a particle size of 25 nm and a specific surface area of 100 m²/g was supplied by MACKLIN (Beijing, China).

2.2. Fabrication of PA11/SiO₂ Composites

First, the PA11 and SiO₂ were vacuum-dried at 70 °C for 24 h, after which they were melt blended at 205 °C and 50 rpm for 10 min at a certain weight ratio using a mixer (Extruder, Brabender GMBH&Co.KG, Duisburg, Germany). The samples were then pre-pressed at 205 °C and 200 bar pressure for 5 min using a flatbed vulcanizing machine (LHHS 20-170919A, Lina Industrial Co., Ltd., Guangdong, China). Eventually, the PA11/x% SiO₂ (x = 0.5, 1.0, 1.5, 2.0.) composite samples were obtained by continued cold pressing at 25 °C and 100 bar for 10 min, where x% represents the mass fraction of the SiO₂ in PA11.

2.3. Morphology Characterization

Scanning electron microscopy (SEM, SU8010, HITACHI, Hitachi City, Japan) and Transmission Electron Microscopy (TEM, Tecnai G2 F20, FEI, Sarum, OR, USA) were conducted to analyze the morphology of the prepared composites. Ultramicrotome (EM UC6, Leica, Wetzlar, Germany) was used to prepare the specimens with a thickness of ~100 nm for the TEM investigation.

2.4. Structure Characterizations

Infrared spectra of the composites were recorded with a Fourier transform infrared spectrometer (FTIR, Tensor II, Bruker, Billica, MA, USA) between 4000 and 600 cm^{-1} . X-ray diffraction (XRD) analysis was conducted on a Bruker D8 Focus X-ray diffractometer by a solid detector and Cu K α radiation. The 2θ ranges were from 5° to 40° at a rate of 5°/min.

2.5. Thermal Analysis

The non-isothermal crystallization behavior in the melts of the composites were performed by using a differential scanning calorimeter (DSC, 204F1, Netzsch, Berlin, Germany). To eliminate thermal history, the samples were first heated from 30 to 205 °C at 20 °C min^{-1} , held at the high temperature for 5 min, and then cooled to 20 °C at 10 °C min^{-1} . After this thermal treatment, the samples were heated from 20 °C to 200 °C at 10 °C min^{-1} for analysis (2nd scan). The crystallization temperature (T_c) and the enthalpy of crystallization (ΔH_c) were measured during the cooling scan. The melting temperature (T_m) and the enthalpy of fusion (ΔH_m) were measured during the 2nd scanning process. The crystallinity (X_m) was estimated according to Equation (1):

$$X_m(\%) = \left(\frac{\Delta H_m}{\Delta H_0} \right) \times 100\% \quad (1)$$

where ΔH_m and ΔH_0 denote the heats (J/g) of melting of the PA11/SiO₂ composites and PA11 crystals of infinite size with a value of 225.9 J/g [22].

Thermogravimetric analysis (TGA) was conducted with a DTA-TG apparatus (DTG-60, SHIMADZU, Kyoto, Japan) ranging from 50 °C to 700 °C with a heating rate of 10 °C/min in a N₂ atmosphere (flow rate 100 mL min^{-1}).

2.6. Mechanical Properties

The mechanical performance was obtained with an Instron machine (WDL-5000N, Daochun, Yangzhou, China) at a strain speed of 50 mm min^{-1} . The samples were cut into 15 × 2 mm dumbbell shapes.

Dynamic mechanical analysis (DMA) was performed using a DMA apparatus (Q800, TA INSTRUMENTS, New Castle, PA, USA) over a temperature range of −20 °C to 100 °C (3 °C min^{-1} , 1 Hz), which covers the temperature range of the PA11 used for flexible riser inner sheaths. The tests were carried out in tension mode. The DMA measurement was used to determine the viscoelastic properties of the tested materials, such as storage modulus (E'), loss modulus (E''), and damping parameter ($\tan \delta$) [23].

2.7. Gas Barrier Test

The applicable temperature range of PA11 is from −20 °C to 90 °C, according to ISO 13628-2017 (Petroleum and natural gas industries—design and operation of subsea production systems Part 11: Flexible pipe systems for subsea and marine applications). The samples with a thickness of approximately 0.5 mm were placed in the permeability unit test apparatus. The low-pressure ends of the composite materials were supported by breathable steel, so that the increase in pressure would not cause deformation failure. The experimental temperature was far lower than the aging temperature of the materials, which will not cause material failure. The input pressure for the test was 4 MPa, and the test temperatures were 20 °C, 30 °C, 50 °C, 70 °C, and 90 °C. Gas permeation tests were conducted according to the corresponding standard GB/T 40260-2021 (Test method for

determining gas permeability of polymer membrane materials), and different batches of the samples were used to test the gas permeability.

The permeation of gas molecules into the polymer was divided into three stages [24], as shown in Figure 2. The first stage was the impermeable state, where the gas molecules collided with the polymer surface. After the transient (unsteady) permeation state, the steady-state permeation state was finally reached, where the diffusion was stable, due to the complete saturation of the internal volume. The permeability coefficient (P) and diffusion coefficient (D) were calculated according to the permeability curve through Equations (2) and (3), respectively [25–27]:

$$\frac{dQ}{dt} = P \times A \times (P_1 - P_2)/h \quad (2)$$

$$D = \frac{h^2}{6\tau} \quad (3)$$

where A denotes the permeated area, P_1 and P_2 stand for high-end and low-end pressure, and h and τ refer to the thickness of the samples and lag time, respectively.

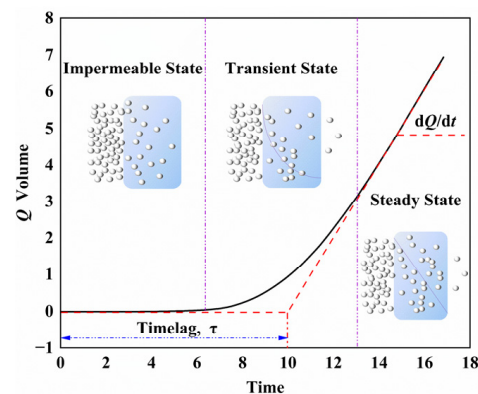


Figure 2. Gas permeate volume curve with time.

3. Results and Discussion

3.1. Morphology Characterization

SEM images for the pure PA11 and the PA11/SiO₂ composite cross-sections are shown in Figure 3. The distribution of the SiO₂ in the PA11 matrix was almost uniform with less agglomeration (the red circle in Figure 3c–f). In addition, the SEM image shows that the sample was flat and free of defects, which ensured the reliability of the mechanical properties and gas permeate behavior tests.

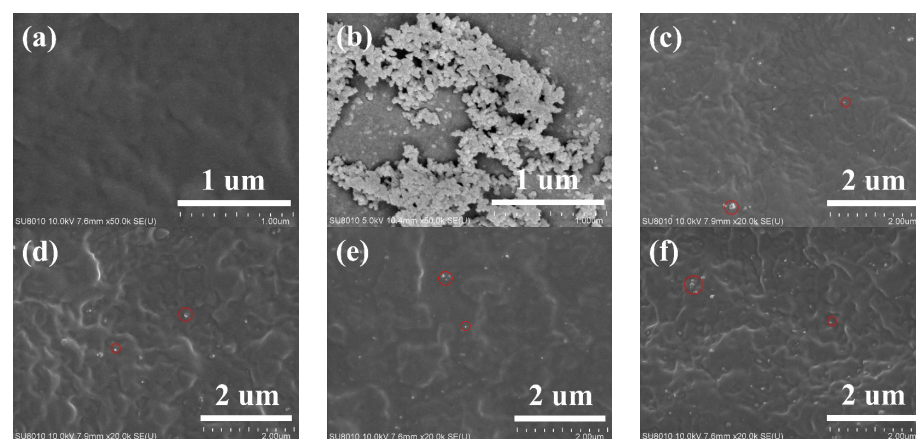


Figure 3. SEM images of composite with different SiO₂ contents: (a) PA11, (b) SiO₂, (c) PA11/0.5% SiO₂, (d) PA11/1.0% SiO₂, (e) PA11/1.5% SiO₂, (f) PA11/2.0% SiO₂.

TEM was performed to further investigate the distribution morphology of the SiO₂. The SiO₂ nanoparticles had a round structure and a size of 25–35 nm, as shown in Figure 4a. For the PA11/SiO₂ composites, the dispersion of the SiO₂ particles in the PA11 matrix was more uniform when the addition amount of nanoparticles was low (below 1.0%), as shown in Figure 4b,c. When the addition was increased to 1.5%, there was a certain degree of nanoparticle agglomeration in the PA11, with a size of about 5 μm, as shown in Figure 4d.

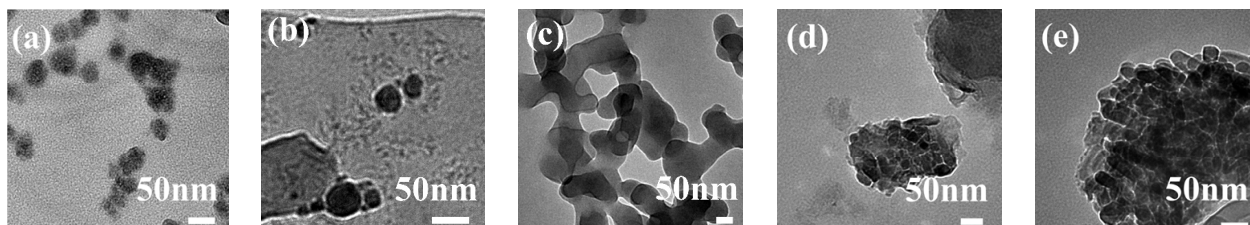


Figure 4. TEM images PA11/SiO₂ composite, (a) SiO₂, (b) PA11/0.5% SiO₂, (c) PA11/1.0% SiO₂, (d) PA11/1.5% SiO₂, (e) PA11/2.0% SiO₂.

3.2. DSC Characterization

It was assumed that the gas penetration in the polymers occurred in the amorphous zone rather than in the crystalline region, which is a limited region [28]. To investigate the impact of the SiO₂ incorporation on the melting and crystallization behaviors of the PA11, DSC tests were performed on the pure PA11 and PA11/SiO₂ composites, as shown in Figure 5. As summarized in Table 1, the T_c of the neat PA11 was 153.3 °C. With the addition of the SiO₂ nanoparticles, the T_c values of the composites improved, demonstrating that SiO₂ acted as a nucleating agent for the PA11 crystallization and increased the crystallization rate [29,30]. Furthermore, the addition of a small amount of SiO₂ had no significant effect on the crystallinity of the PA11.

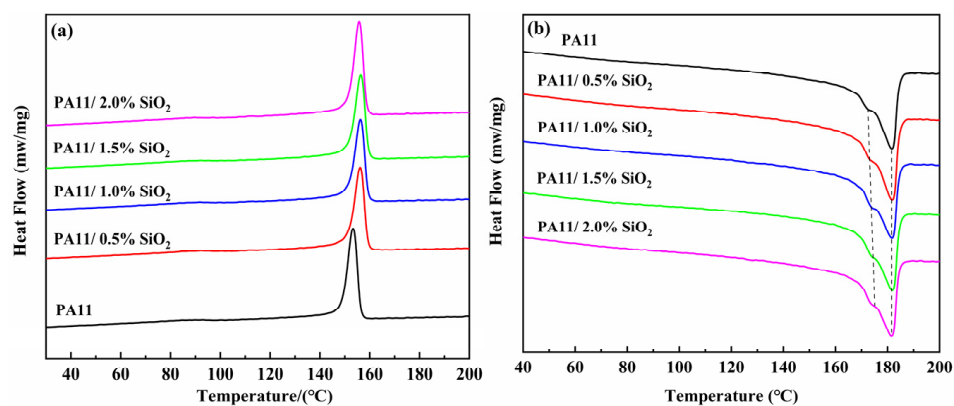


Figure 5. DSC curves of PA11/SiO₂ composites: (a) crystallization curve, (b) melting curve.

Table 1. DSC thermodynamic parameters of PA11/SiO₂ composites.

Sample	$T_c/^\circ\text{C}$	$\Delta H_c/\text{J}\cdot\text{g}^{-1}$	$T_m/^\circ\text{C}$	$\Delta H_m/\text{J}\cdot\text{g}^{-1}$	$X_c/\%$
PA11	153.3	52.50	181.7	53.39	23.63
PA11/0.5% SiO ₂	156.1	54.00	181.8	54.50	24.13
PA11/1.0% SiO ₂	156.3	51.67	181.7	52.23	23.13
PA11/1.5% SiO ₂	156.4	52.98	181.9	53.67	23.76
PA11/2.0% SiO ₂	155.8	53.48	181.7	54.54	24.15

This was mainly attributed to the potent intrinsic hydrogen bonding network that is typical of polyimides, which stabilized the PA11 amorphous phase [31]. For melting curves, all PA11/SiO₂ composite samples showed two melting peaks, which can be attributed to

the fusion of different types of crystals in the semi-crystallized PA11. The melting peaks at higher temperatures might be attributed to the melting of the perfect crystals, whereas the melting peaks at lower temperatures could be assigned to the deficient crystals produced by short molecular chains [32,33].

3.3. Structure Characterization

The crystal structures of the PA11 and PA11/SiO₂ nanocomposites were characterized by XRD, as presented in Figure 6. The main crystalline peaks in the XRD spectra were observed at $2\theta = 7^\circ$, 20.5° , and 23.5° , which corresponded to the α -polymorph of the PA11 [34]. Moreover, the addition of the SiO₂ did not affect the crystal structure of the PA11.

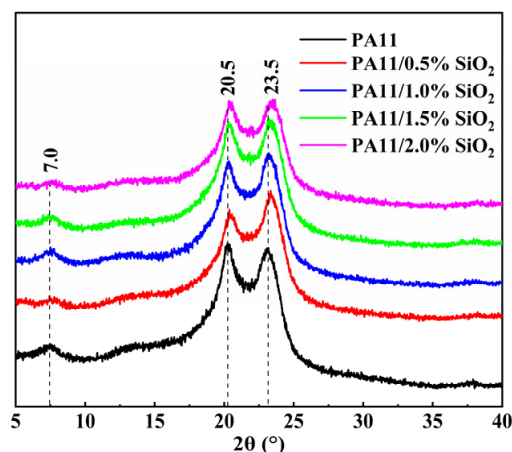


Figure 6. XRD spectra of PA-11 and PA11/SiO₂ composites.

The structures of the PA11, SiO₂, and PA11/SiO₂ composites were characterized by FTIR (Figure 7). In the curve of the PA11, the bands at 1635 and 1539 cm^{-1} corresponded to the C=O stretching vibration and N-H bending vibration, respectively [6,35–40]. The peaks at 806 cm^{-1} and 1105 cm^{-1} indicated the anti-symmetric stretching and asymmetric stretching vibrations of the Si-O-Si, respectively [41,42]. The area ratio of absorption bands at 1091 cm^{-1} (A_{1091}) and 806 cm^{-1} (A_{806}) to 1635 cm^{-1} (A_{1635}) exhibited the relative amounts of Si-O-Si groups in the composites. As shown in Figure 7g, compared with the PA11, the peak area ratios of the $A_{1091}/1635$, and $A_{806}/1635$ increased with the SiO₂ additive amount, which demonstrated the successful introduction of the SiO₂ into the PA11 matrix.

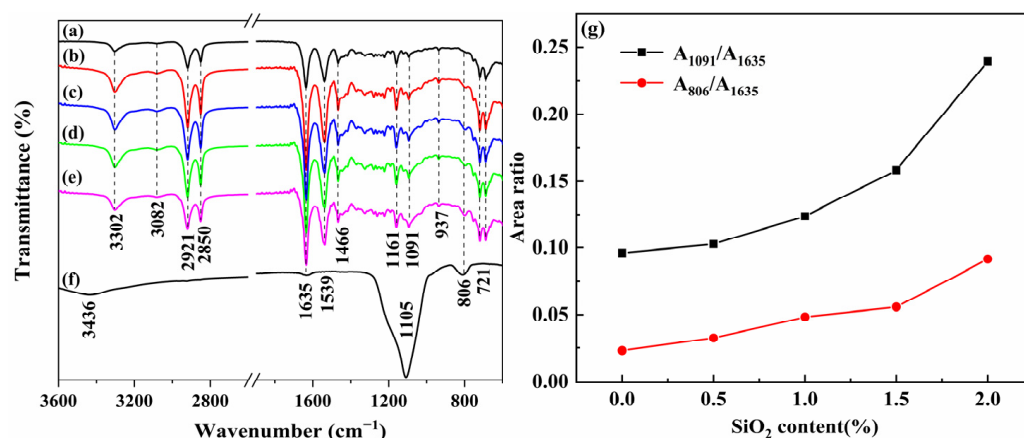


Figure 7. FTIR spectra of PA11 and PA11/SiO₂ composites: (a) PA11, (b) PA11/0.5% SiO₂, (c) PA11/1.0% SiO₂, (d) PA11/1.5% SiO₂, (e) PA11/2.0% SiO₂, (f) SiO₂, (g) A_{1091}/A_{1635} and A_{806}/A_{1635} ratios of FTIR peak areas.

3.4. Mechanical and Thermal Stability Characterization

Figure 8 depicts the stress–strain curves of the PA11 and PA11/SiO₂ composites. The mechanical properties determined from the curves are shown in Table 2. The neat PA11 had a tensile strength of 78.4 MPa, an elasticity modulus of 89.9 MPa, and a break elongation of 447.7%. As the SiO₂ content increased, the nanoscale SiO₂ aggregated and existed in the form of defects in the PA11/SiO₂ composites, which reduced the tensile strengths and break elongations of the composites to some extent. When compared to the pristine PA11, the presence of SiO₂ in the PA11 resulted in a higher elasticity modulus and a decrease in the break elongation. The findings are consistent with previous research [43,44].

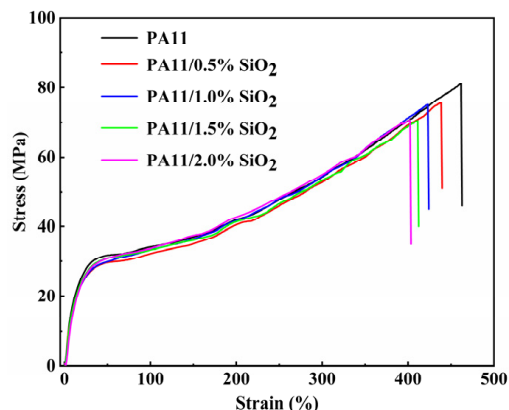


Figure 8. The stress–strain curves of PA11 and PA11/SiO₂ composites.

Table 2. Mechanical properties of PA11/SiO₂ composites.

Sample	Tensile Strength (MPa)	Elongation at Break (%)	Elasticity Modulus (MPa)
PA11	78.5 ± 3.6	447.7 ± 12.7	89.9 ± 4.6
PA11/0.5%SiO ₂	74.1 ± 2.3	425.6 ± 16.6	92.7 ± 9.8
PA11/1.0%SiO ₂	73.9 ± 3.0	413.8 ± 9.9	97.2 ± 7.4
PA11/1.5%SiO ₂	72.0 ± 2.7	406.9 ± 12.5	97.9 ± 3.7
PA11/2.0%SiO ₂	71.0 ± 2.1	399.1 ± 13.5	97.4 ± 8.8

The mechanical properties of the PA11 and nanocomposites were further studied by dynamic mechanical analysis (DMA). The changes in the energy storage modulus (E') and loss modulus (E'') with temperature are shown in Figure 9. E' and E'' increased above or below the glass transition temperature (T_g). Changes below the T_g were greater than those above the T_g . This result was consistent with other studies on polymer nanocomposites reinforced by nanomaterials [30,45].

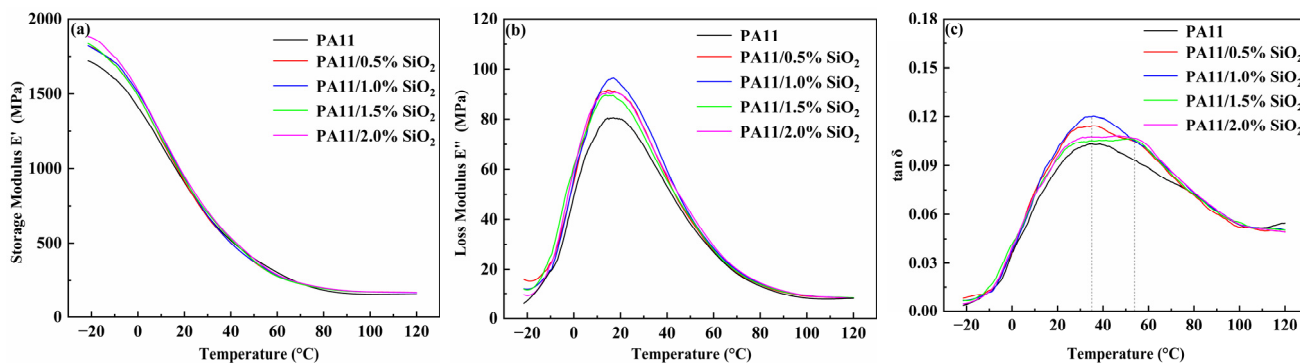


Figure 9. (a) Storage modulus, (b) loss modulus, and (c) tan δ of neat PA11 along with PA11/SiO₂ composites.

When the PA11 was in the glassy state rather than the rubber state, the effect of the nanoparticles was more significant. The relaxation of the PA11 and nanocomposites was studied using $\tan \delta$ data shown in Figure 9c. For the T_g -associated α relaxation centered at 35–40 °C, there was a transition to a higher temperature in many nanocomposite samples. The SiO₂ may have reduced the free volume in the PA11 by hindering the chain movement and conformation change. In addition, at the high SiO₂ content in Figure 9c, the $\tan \delta$ peak became wider, and a second higher T_g was observed, showing that the molecular chain movement of the PA11 was restricted, resulting in a large realistic response of the nanocomposites [46–48].

TGA and DTG were performed to test the thermal stability of the neat PA11 and the nanocomposites with nitrogen airflow (Figure 10a,b). All the tested materials showed two main weight losses, at 280 °C and 460 °C. The first degradation step, with a shallow peak in the DTG curve centered at around 280 °C, was attributed to the decarboxylation process [49]. In the second degradation step, a main peak was identified in the DTG curves. On the other hand, the melting temperature of SiO₂ was over 1600 °C. Thus, it was inferred that the degradation occurred due to the decomposition of the PA11 backbones.

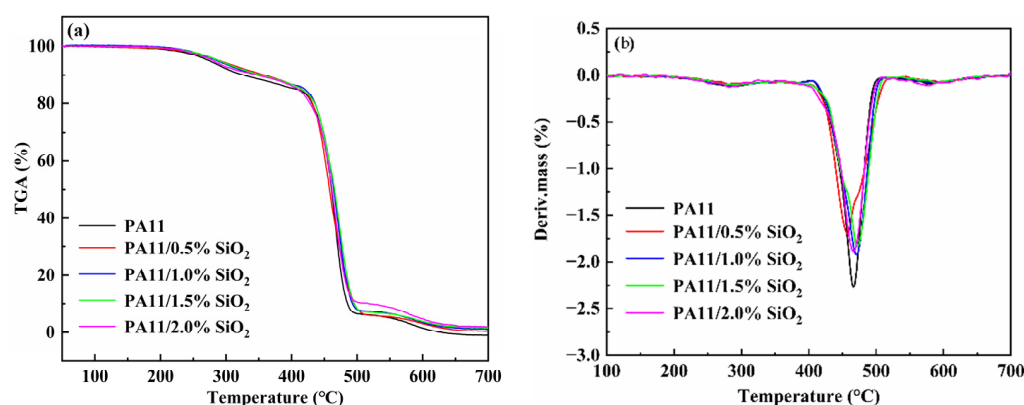


Figure 10. TGA curves (a) and DTG curves (b) of neat PA11 and PA11/SiO₂ composites.

3.5. CO₂ Permeability Characterization and Behavior Analysis

For vertical two-phase flow in pipes, the common flow patterns are annular flow, slug flow, bubble flow, and dispersed bubble flow [50]. The multiphase flow pattern has a significant effect on the temperature and pressure distribution of the flexible riser, which in turn affects the rate of gas phase permeation into the annulus within the flexible riser. Flexible risers are usually required for long-term service and therefore require an in-depth study of the steady-state permeation processes. The CO₂ permeabilities of the PA11 and PA11/SiO₂ composites were measured at 20 °C, 30 °C, 50 °C, 70 °C, and 90 °C. These temperatures were chosen because they are typical values for PA11 applications in flexible risers. In addition, the design of the temperatures involved two states of the PA11, the glassy state and the rubbery state. Figure 11 displays the results of the permeation coefficients for the PA11/SiO₂ composites, each averaged over four parallel specimens from different batches. The test data error of different samples in the same batch and the error of different samples was calculated, which can meet the requirement of 5.0% of the standard.

The percentage reduction in the permeability coefficient of the PA11/SiO₂ composites compared to the pure PA11 varied at different temperatures. The maximum decreases in the permeability coefficients of the PA11/SiO₂ composites at 20–90 °C were: 17.02% at 20 °C, 13.48% at 30 °C, 9.41% at 50 °C, 8.62% at 70 °C, and 10.87% at 90 °C. It is evident that the percentage difference between the PA11 and PA11/SiO₂ permeability coefficients decreased with increasing temperature. Additionally, as the temperature increased, the increase of nanoparticle content had a greater impact on the permeation behavior of the composites.

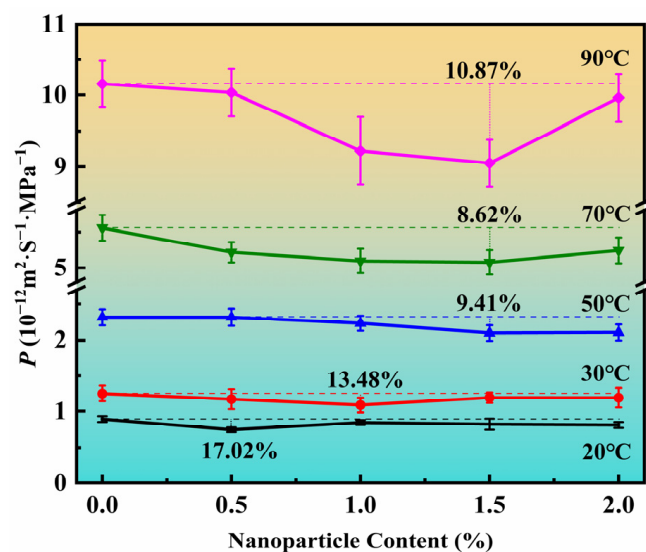


Figure 11. Permeability coefficient of PA11 and PA11/SiO₂ composites at 20 °C, 30 °C, 50 °C, 70 °C, and 90 °C.

To further analyze the influence of the various nanoparticle contents on the behavior of the gas permeation at various temperatures, the activation energies for the diffusion, solubility, and permeation of the composites of PA11/SiO₂ were calculated based on the widely used solution-diffusion model [51,52]. The effect of the temperature on gas diffusion and solubility was expressed by the Arrhenius Equations (4) and (5), respectively [28]:

$$D = D_0 \times \exp\left(-\frac{E_D}{RT}\right) \quad (4)$$

$$S = S_0 \times \exp\left(-\frac{\Delta H_S}{RT}\right) \quad (5)$$

where D_0 is the pre-exponential factor and E_D is the activation energy of diffusion; ΔH_S is the partial molar enthalpy of sorption. T is the temperature (K), and R is the ideal gas constant. Hence, the permeability can be obtained by multiplying the solubility coefficient (a thermodynamic coefficient) by the diffusivity coefficient (a kinetic coefficient), and the gas permeability as a function of temperature was obtained using Equation (6) [53–55]:

$$P = P_0 \times \exp\left(-\frac{E_P}{RT}\right) \quad (6)$$

where P_0 is the pre-exponential factor and E_P is the activation energy of permeation. In general, permeability increases with increasing temperature. The values of E_D and E_P were determined for each gas from the slopes of the $\ln(D)$ and $\ln(P)$ vs. $1000/T$ curves (Figures S1 and S2, Tables S1 and S2), respectively. The distinction between the E_P and E_D was represented by ΔH_S and is summarized in Table 3.

Table 3. Apparent activation energies for permeability, diffusion, and heat of solution of CO₂ in PA11.

Samples	PA11	PA11/ 0.5% SiO ₂	PA11/ 1.0% SiO ₂	PA11/ 1.5% SiO ₂	PA11/ 2.0% SiO ₂	Reference
E_P (kJ/mol)	31.94	32.81	30.63	30.99	31.08	35 [28], 34 [56]
E_D (kJ/mol)	45.74	46.17	46.22	50.79	48.40	40 [28], 52 [56]
ΔH_S (kJ/mol)	−13.80	−13.36	−15.58	−19.80	−17.31	(−10)–(−4) [28] (−18)–(−13) [56]

E_D increased with the increase in the nanoparticle content, indicating the diffusion of gas molecules was more difficult. ΔH_S was negative, showing that gas dissolution was an exothermic process, whereas E_P and E_D were positive, suggesting that the permeation and diffusion were heat-absorbing processes. As temperature increased, the permeability and diffusion coefficients of the PA11 to CO₂ increased, whereas the solubility coefficient exhibited the opposite trend, as shown in Figure S3.

Gas permeation is closely related to the state of motion of the polymer. The free volume theory of gas diffusion in glass polymers proposed by Vrentas and Duda [57,58] assumes the existence of pores, i.e., free volumes, between polymer chain segments. Gas molecules jump from one free volume unit to the next to complete the diffusion process. To achieve this process, gas molecules need to have sufficiently large free volume units in adjacent positions and sufficient energy to overcome the jump resistance. Figure S4 depicts the variation pattern of the free volume with temperature and shows an obvious distinction in the permeation curves of the composites in the glass and rubber states. When the polymer was in the glassy state, the chain segment motion was in a frozen state, and no conformational changes could occur; the chain segment spacing formed during the thermal movement of the molecular chain segments was the main channel for gas diffusion [59].

In the glassy state, gas molecules had high resistance to jumping between free volumes, and the solubility had a large effect on the permeability coefficient. As shown in Figure 4, the 0.5% proportion of nanoparticles efficiently dispersed and occupied the free volume of the PA11, thus reducing the free volume (Figure 12a) and solubility. The uniformly dispersed nanoparticles could also simultaneously extend the diffusion paths of the gas molecules. As a result, the highest reduction in the PA11/0.5% SiO₂ composite permeability coefficient occurred at 20 °C below the glass transition temperature. As the nanoparticle content increased, the nanoparticles began to agglomerate and fill the free volume, resulting in gaps and increasing solubility. The ΔH_S values in Table 3 showed the same pattern.

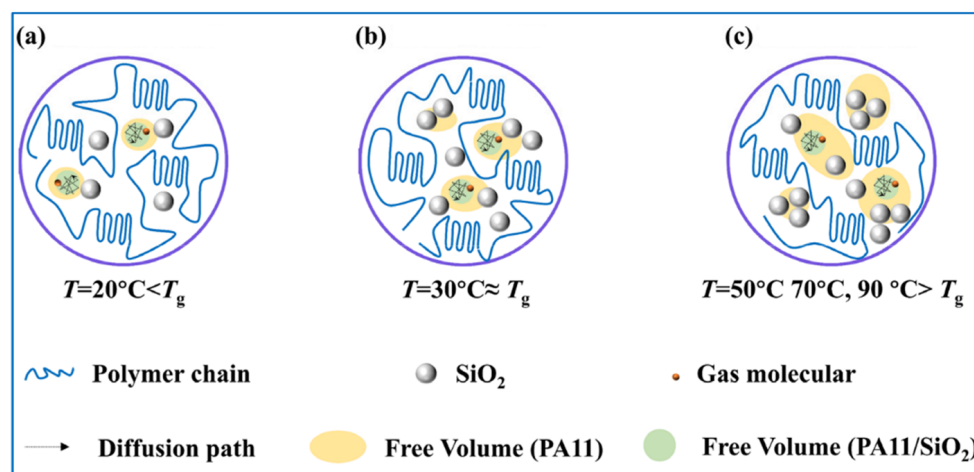


Figure 12. Diffusion paths of gas molecules and influence of nanoparticles on free volume at different temperatures, (a) PA11/0.5% SiO₂, (b) PA11/1.0% SiO₂, (c) PA11/1.5% SiO₂.

When the temperature gradually increased, the chain segments were unfrozen from the frozen state. In the rubbery state case, the free volume increased, and the gas molecules had low resistance to jumping. The larger free volume meant that more nanoparticles were needed to effectively inhibit the increase in permeability caused by the increase in free volume (Figure 12c). The E_D increased as the nanoparticle content rose, indicating that diffusion was difficult, and that the presence of nanoparticles slowed down the movement of the molecular chains while extending the diffusion path. When the content of nanoparticles was greater than 1.5%, the activation energy decreased, due to agglomeration diffusion. Therefore, the PA11/1.5% SiO₂ composite exhibited the lowest permeability coefficient in the rubbery state.

4. Conclusions

In this study, the PA11/SiO₂ composites were made by vacuum densification and mixing in a range of proportions. The DMA results demonstrated that the presence of nanoparticles impeded the mobility of the molecular chains. It is evident from the CO₂ permeation performance tests carried out at 20 °C, 30 °C (the glassy state), 50 °C, 70 °C, and 90 °C (the high elasticity state) that when the temperature rose from 20 °C to 90 °C, the amount of SiO₂ that displayed the lowest permeability coefficient rose. When the composites were in a glass state, the solubility had the greatest influence on the permeability behavior. The uniformly dispersed nanoparticles made the molecular diffusion path longer, which had an obvious blocking effect. At 20 °C, the permeability coefficient of the PA11/0.5% SiO₂ composite decreased by 17.02% compared with that of the PA11. When the composite was in the rubber state, more nanoparticles were required to inhibit the permeability increase caused by the increase in free volume. However, when the nanoparticles aggregated, the diffusion coefficient increased. Therefore, the permeability coefficient of the PA11/1.5% SiO₂ composite in the rubbery state was the lowest. The PA11/SiO₂ composites exhibited strong potential for use as flexible risers with high barrier performance.

Supplementary Materials: The following supporting information can be downloaded at: <https://www.mdpi.com/article/10.3390/polym14204260/s1>, Figure S1: Temperature influence on transport coefficients of CO₂ in PA11/SiO₂ composite, Permeability versus reciprocal temperature; Figure S2: Temperature influence on transport coefficients of CO₂ in PA11/SiO₂ composite, diffusion versus reciprocal temperature; Figure S3: Permeability coefficient, diffusion coefficient, and solubility of CO₂ in PA11 vary with temperature; Figure S4: Permeation curve of PA11 at 20 °C, 30 °C, 50 °C, 70 °C, and 90 °C, diagram of free volume with temperature; Table S1: Intercept and slope of permeability–temperature fitting curve; Table S2: Intercept and slope of diffusion–temperature fitting curve.

Author Contributions: Conceptualization, J.W. and D.H.; methodology, J.W. and X.Z.; validation, Q.Z., Y.L. and X.M.; formal analysis, J.W.; investigation, J.W. and C.C.; resources, D.H.; data curation, X.M. and C.C.; writing—original draft preparation, J.W.; writing—review and editing, X.M. and D.H.; visualization, X.Z.; supervision, X.Y. and Q.Z.; project administration, Q.Z. All authors have read and agreed to the published version of the manuscript.

Funding: This work was supported by the science and technology project of CNOOC (China) Co., LTD. “Research on Fluid Penetration Simulation and Control Technology of Deepwater Oil and Gas Transmission Hose”, (Grant No. 2020-YXKJ-013).

Institutional Review Board Statement: Not applicable.

Informed Consent Statement: Not applicable.

Data Availability Statement: Not applicable.

Conflicts of Interest: The authors declare no conflict of interest.

References

1. Martins, O.D.C.; Souza, R.R.; Lima, R.S.T.; Reguly, A. Development of micromagnetic techniques for stress analysis in flexible risers. *Rev. Matéria* **2011**, *16*, 613–620.
2. Ossai, C.I.; Boswell, B.; Davies, I.J. Pipeline failures in corrosive environments—A conceptual analysis of trends and effects. *Eng. Fail. Anal.* **2015**, *53*, 36–58. [[CrossRef](#)]
3. Tiu, B.; Advincula, R.C. Polymeric corrosion inhibitors for the oil and gas industry: Design principles and mechanism. *React. Funct. Polym.* **2015**, *95*, 25–45. [[CrossRef](#)]
4. Pottmaier, D.; Melo, C.R.; Sartor, M.N.; Kuester, S.; Amadio, T.M.; Fernandes, C.; Marinha, D.; Alarcon, O.E. The Brazilian energy matrix: From a materials science and engineering perspective. *Renew. Sustain. Energy Rev.* **2013**, *19*, 678–691. [[CrossRef](#)]
5. Frederico, G.D.A.; Veiga, A.G.; da CP Gomes, A.P.A.; da Costa, M.F.; Rocco, M.L.M. Using XPS and FTIR spectroscopies to investigate polyamide 11 degradation on aging flexible risers—ScienceDirect. *Polym. Degrad. Stab.* **2021**, *195*, 109787.
6. Simek, J.; Dockalova, V.; Hrdlicka, Z.; Duchacek, V. Effect of liquid butadiene rubber on mechanical properties of polyamide 11/polyamide 12 blends. *J. Polym. Eng.* **2015**, *35*, 349–357. [[CrossRef](#)]
7. Liu, T.; Lim, K.P.; Tjiu, W.C.; Pramoda, K.P.; Chen, Z.K. Preparation and characterization of nylon 11/organoclay nanocomposites. *Polymer* **2003**, *44*, 3529–3535. [[CrossRef](#)]

8. Wang, B.B.; Hu, G.S.; Zhao, X. Preparation and characterization of nylon 6 11 copolymer. *Mater. Lett.* **2006**, *60*, 2715–2717. [[CrossRef](#)]
9. Mago, G.; Kalyon, D.M.; Fisher, F.T. Nanocomposites of polyamide-11 and carbon nanostructures: Development of microstructure and ultimate properties following solution processing. *J. Polym. Sci. Part B Polym. Phys.* **2011**, *49*, 1311–1321. [[CrossRef](#)]
10. Moshynets, O.; Bardeau, J.F.; Tarasyuk, O.; Makhno, S.; Cherniavska, T.; Zhuzha, O.D.; Potters, G.; Rogalsky, S. Antibiofilm Activity of Polyamide 11 Modified with Thermally Stable Polymeric Biocide Polyhexamethylene Guanidine 2-Naphtalenesulfonate. *Int. J. Mol. Sci.* **2019**, *20*, 348. [[CrossRef](#)]
11. Zhan, H.; Nie, Y.; Chen, Y.; Bell, J.M.; Gu, Y. Thermal transport in 3D nanostructures. *Adv. Funct. Mater.* **2020**, *30*, 1903841. [[CrossRef](#)]
12. Naskar, A.K.; Keum, J.K.; Boeman, R.G. Polymer matrix nanocomposites for automotive structural components. *Nat. Nanotechnol.* **2016**, *11*, 1026–1030. [[CrossRef](#)] [[PubMed](#)]
13. Anguita, J.V.; Smith, C.; Stute, T.; Funke, M.; Silva, S. Publisher Correction: Dimensionally and environmentally ultra-stable polymer composites reinforced with carbon fibres. *Nat. Mater.* **2020**, *19*, 317–322. [[CrossRef](#)] [[PubMed](#)]
14. Medeiros, D.; Jardim, P.; de Tatagiba, M.; d’Almeida, J. Composites of recycled nylon 11 and titanium based nanofillers. *Polym. Test.* **2015**, *42*, 108–114. [[CrossRef](#)]
15. Petrovicova, E.; Knight, R.; Schadler, L.S.; Twardowski, T.E. Nylon 11/silica nanocomposite coatings applied by the HVOF process. II. Mechanical and barrier properties. *J. Appl. Polym. Sci.* **2015**, *78*, 2272–2289. [[CrossRef](#)]
16. Rodrigues, A.D.C.; Bastos, I.N.; Kappel, M.A.A.; Nascimento, C.R.; Ferreira, L.S.; da Silva, A.L.N. Micromechanical Property Study of Nylon 11 and Organoclay Systems for Offshore Flexible Pipe. *Fibers Polym.* **2021**, *22*, 3172–3182. [[CrossRef](#)]
17. Da Cruz, B.D.S.M.; Tienne, L.G.P.; Gondim, F.F.; Candido, L.d.; Chaves, E.G.; Marques, M.D.F.V.; da Luz, F.S.; Monteiro, S.N. Graphene nanoplatelets reinforced Polyamide-11 nanocomposites thermal stability and aging for application in flexible pipelines. *J. Mater. Res. Technol.* **2022**, *18*, 1842–1854. [[CrossRef](#)]
18. Santos, B.P.S.; Arias, J.J.R.; Jorge, F.E.; Santos, R.E.P.D.; Fernandes, B.S.; Candido, L.D.; Peres, A.C.D.; Chaves, E.G.; Marques, M.D.F.V. Preparation, characterization and permeability evaluation of poly (vinylidene fluoride) composites with ZnO particles for flexible pipelines. *Polym. Test.* **2021**, *94*, 107064. [[CrossRef](#)]
19. Santos, B.P.S.; Arias, J.J.R.; Jorge, F.E.; Santos, R.E.P.D.; Gondim, F.F.; Fernandes, B.S.; Candido, L.S.; Peres, A.C.C.; Gervasoni, E.; Marques, M.D.V. Synthesis and characterization of poly(vinylidene fluoride) composites with flower-like ZnO particles for flexible pipelines applications. *J. Mater. Res. Technol.* **2021**, *13*, 99–110. [[CrossRef](#)]
20. Santos, B.P.S.; Arias, J.J.R.; Jorge, F.E.; Santos, R.E.P.D.; Fernandes, B.S.; Candido, L.S.; Peres, A.C.C.; Chaves, E.G.; Marques, V.M.F. PVDF containing different oxide nanoparticles for application in oil and gas pipelines. *Mater. Today Commun.* **2021**, *26*, 101743. [[CrossRef](#)]
21. Gondim, F.F.; Tienne, L.; Cruz, B.; Chaves, E.G.; Marques, M.V. Poly(vinylidene fluoride) with zinc oxide and carbon nanotubes applied to pressure sheath layers in oil and gas pipelines. *J. Appl. Polym. Sci.* **2020**, *138*, 50157. [[CrossRef](#)]
22. Wang, B.; Wang, L.; Wang, Y.; Zhou, Z. Unusual toughening effect of graphene oxide on the graphene oxide/nylon 11 composites prepared by in situ melt polycondensation. *Compos. Part B Eng.* **2013**, *55*, 215–220. [[CrossRef](#)]
23. Lebaupin, Y.; Chauvin, M.; Hoang, T.-Q.T.; Touchard, F.; Beigbeder, A. Influence of constituents and process parameters on mechanical properties of flax fibre-reinforced polyamide 11 composite. *J. Thermoplast. Compos. Mater.* **2016**, *30*, 1503–1521. [[CrossRef](#)]
24. Wijmans, J.G.; Baker, R.W. The solution-diffusion model: A review. *J. Membr. Sci.* **1995**, *107*, 1–21. [[CrossRef](#)]
25. Bastani, D.; Esmaeili, N.; Asadollahi, M. Polymeric mixed matrix membranes containing zeolites as a filler for gas separation applications: A review. *J. Ind. Eng. Chem.* **2013**, *19*, 375–393. [[CrossRef](#)]
26. Amooghin, A.E.; Shehni, P.M.; Ghadimi, A.; Sadrzadeh, M.; Mohammadi, T. Mathematical modeling of mass transfer in multicomponent gas mixture across the synthesized composite polymeric membrane. *J. Ind. Eng. Chem.* **2013**, *19*, 870–885. [[CrossRef](#)]
27. Arjmandi, M.; Pakizeh, M. Mixed matrix membranes incorporated with cubic-MOF-5 for improved polyetherimide gas separation membranes: Theory and experiment. *J. Ind. Eng. Chem.* **2014**, *20*, 3857–3868. [[CrossRef](#)]
28. Flaconneche, B.; Martin, J.; Klopffer, M.H. Permeability, Diffusion and Solubility of Gases in Polyethylene, Polyamide 11 and Poly (Vinylidene Fluoride). *Oil Gas Sci. Technol.* **2001**, *56*, 261–278. [[CrossRef](#)]
29. Zhang, Q.; Yu, M.; Fu, Q. Crystal morphology and crystallization kinetics of polyamide-11/clay nanocomposites. *Polym. Int.* **2004**, *53*, 1941–1949. [[CrossRef](#)]
30. Peng, S.X.; Shrestha, S.; Youngblood, J.P. Crystal structure transformation and induction of shear banding in Polyamide 11 by surface modified Cellulose Nanocrystals. *Polymer* **2017**, *114*, 88–102. [[CrossRef](#)]
31. Lonjon, A.; Caffrey, I.; Carponcin, D.; Dantras, E.; Lacabanne, C. High electrically conductive composites of Polyamide 11 filled with silver nanowires: Nanocomposites processing, mechanical and electrical analysis. *J. Non-Cryst. Solids* **2013**, *376*, 199–204. [[CrossRef](#)]
32. Hua, Z.; Shi, X.; Chen, Y. Preparation, structure, and property of highly filled polyamide 11/BaTiO₃ piezoelectric composites prepared through solid-state mechanochemical method. *Polym. Compos.* **2017**, *40*, 177–185.
33. Wan, J.; Bu, Z.Y.; Li, C.; Hong, F.; Li, B.G. Preparation, melting, glass relaxation and nonisothermal crystallization kinetics of a novel dendritic nylon-11. *Thermochim. Acta* **2011**, *524*, 117–127. [[CrossRef](#)]
34. Dechet, M.A.; Goblirsch, A.; Romeis, S.; Zhao, M.; Lanyi, F.J.; Kaschta, J.; Schubert, D.W.; Drummer, D.; Peukert, W.; Schmidt, J. Production of polyamide 11 microparticles for Additive Manufacturing by liquid-liquid phase separation and precipitation. *Chem. Eng. Sci.* **2019**, *197*, 11–25. [[CrossRef](#)]
35. Huang, Y.Q.; Dai, D.D.; Li, H.B.; Sun, L.; Runt, J.; Huang, K.S.; Yeh, J.T. Oxygen barrier, free volume, and blending properties of fully bio-based polyamide 11/poly(vinyl alcohol) blends. *J. Appl. Polym. Sci.* **2019**, *137*, 48562. [[CrossRef](#)]

36. Domingos, E.; Pereira, T.M.C.; Castro, E.V.R.D.; Romao, W.; Guimaraes, R.C.L. Monitoring the Degradation of Polyamide 11 (PA-11) via Fourier Transform Infrared Spectroscopy (FTIR). *Polimeros* **2013**, *23*, 37–41. [[CrossRef](#)]
37. Yang, X.; Wang, H.; Chen, J.; Fu, Z.; Zhao, X.; Li, Y. Copolymers containing two types of reactive groups: New compatibilizer for immiscible PLLA/PA11 polymer blends. *Polymer* **2019**, *177*, 139–148. [[CrossRef](#)]
38. Jubinville, D.; Chang, B.P.; Pin, J.-M.; Mohanty, A.K.; Misra, M. Synergistic thermo-oxidative maleation of PA11 as compatibilization strategy for PA6 and PBT blend. *Polymer* **2019**, *179*, 121594. [[CrossRef](#)]
39. Halim, K.; Farrell, J.B.; Kennedy, J.E. Preparation and characterisation of polyamide 11/montmorillonite (MMT) nanocomposites for use in angioplasty balloon applications. *Mater. Chem. Phys.* **2013**, *143*, 336–348. [[CrossRef](#)]
40. Gaabour, L.H. Influence of silica nanoparticles incorporated with chitosan/polyacrylamide polymer nanocomposites. *J. Mater. Res. Technol.* **2019**, *8*, 2157–2163. [[CrossRef](#)]
41. Do, V.-T.; Chun, D.-M. Fabrication of large-scale, flexible, and robust superhydrophobic composite films using hydrophobic fumed silica nanoparticles and polydimethylsiloxane. *Polymer* **2022**, *244*, 124630. [[CrossRef](#)]
42. Ramalla, I.; Gupta, R.K.; Bansal, K. Effect on superhydrophobic surfaces on electrical porcelain insulator, improved technique at polluted areas for longer life and reliability. *Int. J. Eng. Technol.* **2015**, *4*, 509–519. [[CrossRef](#)]
43. Mancic, L.; Pontón, P.I.; Letichevsky, S.; Costa, A.M.; Marinkovic, B.A.; Rizzo, F.C. Application of silane grafted titanate nanotubes in reinforcing of polyamide 11 composites. *Compos. Part B Eng.* **2016**, *93*, 153–162. [[CrossRef](#)]
44. Yamunadevi, V.; Vijayanand, G.; Ganeshan, P.; Sowmiya, S.; Raja, K. Effect on the behaviour of dynamic mechanical analysis for hybrid epoxy nanocomposite. *Mater. Today Proc.* **2020**, *37*, 223–227. [[CrossRef](#)]
45. Nicharat, A.; Sapkota, J.; Weder, C.; Foster, E.J. Melt processing of polyamide 12 and cellulose nanocrystals nanocomposites. *J. Appl. Polym. Sci.* **2015**, *132*, 42752. [[CrossRef](#)]
46. Aroon, M.A.; Ismail, A.F.; Matsuura, T.; Montazer-Rahmati, M.M. Performance studies of mixed matrix membranes for gas separation: A review. *Sep. Purif. Technol.* **2010**, *75*, 229–242. [[CrossRef](#)]
47. Moore, T.T.; Koros, W.J. Non-ideal effects in organic–inorganic materials for gas separation membranes. *J. Mol. Struct.* **2005**, *739*, 87–98. [[CrossRef](#)]
48. Chung, T.S.; Lan, Y.J.; Yi, L.; Kulprathipanja, S. Mixed matrix membranes (MMMs) comprising organic polymers with dispersed inorganic fillers for gas separation. *Prog. Polym. Sci.* **2007**, *32*, 483–507. [[CrossRef](#)]
49. Bugatti, V.; Bernardo, P.; Clarizia, G.; Viscusi, G.; Vertuccio, L.; Gorrasi, G. Ball Milling to Produce Composites Based of Natural Clinoptilolite as a Carrier of Salicylate in Bio-Based PA11. *Polymers* **2019**, *11*, 634. [[CrossRef](#)]
50. Wu, B.; Firouzi, M.; Mitchell, T.; Rufford, T.E.; Leonardi, C.; Towler, B. A critical review of flow maps for gas-liquid flows in vertical pipes and annuli. *Chem. Eng. J.* **2017**, *326*, 350–377. [[CrossRef](#)]
51. Klepić, M.; Jansen, J.C.; Fuoco, A.; Esposito, E.; Izák, P.; Petrusová, Z.; Vankelecom, I.F.; Randová, A.; Fíla, V.; Lanč, M. Gas separation performance of carbon dioxide-selective poly (vinyl alcohol)–ionic liquid blend membranes: The effect of temperature, feed pressure and humidity. *Sep. Purif. Technol.* **2021**, *270*, 118812. [[CrossRef](#)]
52. Rabiee, H.; Alsadat, S.M.; Soltanieh, M.; Mousavi, S.A.; Ghadimi, A. Gas permeation and sorption properties of poly (amide-12-b-ethyleneoxide)(Pebax1074)/SAPO-34 mixed matrix membrane for CO₂/CH₄ and CO₂/N₂ separation. *J. Ind. Eng. Chem.* **2015**, *27*, 223–239. [[CrossRef](#)]
53. Salahshoori, I.; Seyfaee, A.; Babapoor, A.; Neville, F.; Moreno-Atanasio, R. Evaluation of the effect of silica nanoparticles, temperature and pressure on the performance of PSF/PEG/SiO₂ mixed matrix membranes: A molecular dynamics simulation (MD) and design of experiments (DOE) study. *J. Mol. Liq.* **2021**, *333*, 115957. [[CrossRef](#)]
54. Gouveia, A.S.; Yanez, M.; Alves, V.D.; Palomar, J.; Moya, C.; Gorri, D.; Tomé, L.C.; Marrucho, I.M. CO₂/H₂ separation through poly (ionic liquid)–ionic liquid membranes: The effect of multicomponent gas mixtures, temperature and gas feed pressure. *Sep. Purif. Technol.* **2021**, *259*, 118113. [[CrossRef](#)]
55. Zhang, B.; Qiao, J.; Wu, D.; He, X.; Liu, J.; Yi, C.; Qi, S. Enhanced Gas Separation by Free Volume Tuning in a Crown Ether-Containing Polyimide Membrane. *Sep. Purif. Technol.* **2022**, *293*, 121116. [[CrossRef](#)]
56. Ash, R.; Barrer, R.M.; Palmer, D.G. Solubility and transport of gases in nylon and polyethylene. *Polymer* **1970**, *11*, 421–435. [[CrossRef](#)]
57. Vrentas, J.S.; Duda, J.L. Diffusion in polymer–Solvent systems. I. Reexamination of the free-volume theory. *J. Polym. Sci. Polym. Phys. Ed.* **1977**, *15*, 403–416. [[CrossRef](#)]
58. Vrentas, J.S.; Duda, J.L. Diffusion in polymer–Solvent systems. II. A predictive theory for the dependence of diffusion coefficients on temperature, concentration, and molecular weight. *J. Polym. Sci. Polym. Phys. Ed.* **1977**, *15*, 417–439. [[CrossRef](#)]
59. Xiao, Y.; Low, B.T.; Hosseini, S.S.; Chung, T.S.; Paul, D.R. The strategies of molecular architecture and modification of polyimide-based membranes for CO₂ removal from natural gas—A review. *Prog. Polym. Sci.* **2009**, *34*, 561–580. [[CrossRef](#)]